Accepted to Phys. Fluids 10.1063/5.0174937

High-resolution microscale velocity field measurement using light field particle image-tracking velocimetry

Mengtao Gu (顾梦涛)[a], Jian Li (李健)[a*], Md. Moinul Hossain[b], Chuanlong Xu (许传龙)[a*]

[a] National Engineering Research Center of Power Generation Control and Safety, Southeast University, Nanjing, China

[b] School of Engineering, University of Kent, Canterbury, Kent CT2 7NT, UK

* Corresponding authors: *chuanlongxu@seu.edu.cn; eelijian@seu.edu.cn*

Abstract

Light field micro-particle image velocimetry (LF-μPIV) can realize the three-dimensional (3D) microscale velocity field measurement, but the spatial resolution of the velocity field is low. Therefore, this study proposes a high-resolution LF particle image-tracking velocimetry (PIV-PTV) in combination with a cross-validation matching (CVM) algorithm. The proposed method performs motion compensation for the distribution of particle center position based on the low-resolution velocity field achieved by PIV and then conducts the CVM on tracer particles with the nearest neighbor method. The motion compensation reduces the particle displacement during the matching, while the CVM reduces the impact of missing particles on the matching accuracy. Thus, the proposed method enables precise tracking of individual particles at higher particle concentrations and improves the spatial resolution of the velocity field. Numerical simulations were conducted on the 3D displacement field reconstruction. The influence of interrogation window size, particle diameter and concentration were analyzed. Experiments were conducted on the microscale 3D velocity field within the microchannel with right-angle bends. Results indicate that the proposed method provides the high-resolution measurement of the microscale 3D velocity field and improves the precision of the velocity field compared to the PTV at higher particle concentrations. It demonstrates that the proposed method outperforms PIV by 26% in resolution and PTV by 76% in precision at a higher particle concentration of 1.5 particles per microlens.

Keywords： Light field microscopy; Particle image velocimetry; Particle tracking velocimetry Cross-validation matching; Spatial resolution

1 Introduction

Microfluidic chips offer precise control over microfluidic flows by utilizing specialized channel structures, such as the Y-shaped junction and serpentine channel, and enhance the efficiency of heat and mass transfer. Thus, microfluidic chips have been extensively used in various applications including organic synthesis[1-3], chemical analysis[4-6] and chip cooling[7-9]. However, with the continuous advancement of microfluidic chips, the complexity of channel structures has increased and led to complex three-dimensional (3D) microfluidic flows such as the vortex flow[10-12] and droplet flow[13-15]. A high-resolution 3D velocity field measurement technique is necessary for the accurate measurement of high-resolution 3D velocity fields of these complex microfluidic flows as well as for a better understanding of microfluidic heat and mass transfer mechanisms. This understanding, in turn, can facilitate the optimization of channel structures and thus enhance the overall performance of microfluidic chips.

The micro-particle image velocimetry (μPIV) is a commonly used method for characterizing microfluidic flow, which combines the PIV and a microscopic imaging system for achieving non-interference and full-field measurement of microscale velocity fields[16, 17]. Various μPIV techniques are proposed such as confocal scanning μPIV[18, 19], holographic μPIV[20, 21], stereoscopic μPIV[22, 23] and defocused μPIV[24-26]. However, these use complex imaging systems and provide low temporal resolution resulting in the inability to achieve transient velocity field measurement. In contrast, Light field (LF)-μPIV offers a simple solution for measuring the microscale 3D velocity fields through a single LF camera and provides higher temporal resolution[27, 28]. The depth and lateral positions of the tracer particles can simultaneously be recorded under a single exposure with the aid of a microlens array (MLA) between the microscope tube lens and the camera sensor[29]. The tracer particle distribution can be retrieved through volumetric reconstruction

algorithms[30, 31] and the microscale 3D velocity field can then be obtained through cross-correlation (CC) calculation on the reconstructed particle distributions from two successive frames. For the CC calculation, the measurement volume can be divided into multiple interrogation windows, and the CC coefficient of each interrogation window will be calculated to determine the velocity vector [32]. However, to ensure the reliability of the velocity vector, each interrogation window must contain at least four tracer particles[33], which means a minimum of four tracer particles is required for an accurate velocity vector measurement. The reconstruction quality of the particle distribution is also crucial for the 3D velocity measurement. For LF-μPIV, it has been observed that the reconstruction quality decreases with increasing particle concentration and the particle concentration should not be too high to ensure the precision of the velocity field. Typically, a particle concentration of 1-1.5 particles per microlens (ppm), which is equivalent to 0.0015-0.0023 particles per pixel (ppp) is recommended[28, 30, 31, 35]. Also, this concentration is much lower than that of confocal scanning μPIV (i.e., 0.01 ppp)[36]. Therefore, the spatial resolution of the velocity field achieved by the LF-μPIV depends on the particle concentration. To improve the spatial resolution of the velocity field under the constraint of limited particle concentration, it is imperative to track particles individually, thereby generating an equivalent number of velocity vectors to that of tracer particles. This can be achieved by the LF micro-particle tracking velocimetry (μPTV).

The LF-μPTV[37] measures the microscale 3D velocity field through a particle matching algorithm such as the nearest neighbor or relaxation methods. The relaxation method requires expert knowledge due to a large number of adjustable parameters[38] whereas the nearest neighbor method only requires the specification of a fixed search radius based on the maximum displacement[39-41]. However, within a fixed measurement volume, a higher particle concentration leads to a small particle spacing and increases the ratio of particle displacement to particle spacing. This creates additional particles to become visible within the range of particle displacement. As a result, the probability of obtaining valid particle matching through the nearest neighbor method is decreased[38, 42], thus reducing the precision of the velocity field measurement. Consequently, the nearest neighbor method is only suitable for lower particle concentrations around 0.1 ppm[37], which is much lower than those used in LF-μPIV (e.g., 1-1.5 ppm). It is, therefore, important to accurately track individual particles at a higher particle concentration to improve the spatial resolution of the velocity field of the LF-μPTV. The particle matching algorithm such as the Shake the Box approach[43] is based on the temporal consistency of particle displacement and provides a higher matching accuracy at higher particle concentrations. However, it requires multiple successive frames (typically 10 frames or more) for the particle distribution reconstruction, which greatly increases the computational cost. In addition, complex and expensive lasers and high-speed cameras are required to ensure the temporal consistency of particle displacement between the multiple successive frames[43], which is also costly and difficult to implement. Thus, an appropriate solution is required to ensure a high resolution and precision of the velocity field by utilizing two successive frames of the reconstructed particle distributions. This can be achieved by developing a hybrid PIV-PTV algorithm[44, 45] where a low-resolution velocity field can initially be achieved through the PIV, followed by individual particle tracking using the PTV. Also, the distribution of particle center position in the first frame can be adjusted through the motion compensation based on the velocity field of PIV. This can reduce the particle displacement between the adjusted first frame and the original second frame during the matching, thereby improving the accuracy of particle matching with the nearest neighbor method[44, 45]. The actual velocity field can then be obtained by substituting the matching results into the two successive original frames for particle tracking.

The hybrid PIV-PTV algorithm has successfully been used in tomographic PIV/PTV for high-resolution 3D velocity field measurements of macroscopic fluid flows[46]. The LF-μPIV/PTV is a variant of tomographic PIV/PTV[47] and is usually constrained by limited viewing angles[48]. This constraint, however, enlarges the elongation of reconstructed particles and lowers the precision of particle positioning. As a result, the measurement precision of the hybrid PIV-PTV can be adversely affected. Hence, it is crucial to assess the suitability of the hybrid PIV-PTV algorithm for high-resolution measurements in LF-μPIV/PTV. Additionally, the precision of the velocity field obtained by the PIV plays a significant role in motion compensation, thereby impacting the subsequent particle matching accuracy. As the precision of PIV is affected by multiple parameters such as interrogation window size, particle diameter and concentration[33], it is essential to investigate the effects of these parameters on the measurement precision of the hybrid PIV-PTV algorithm.

Furthermore, in LF-μPIV/PTV, the reconstructed particles can be overlapped[31] and lower the particle identification

accuracy, thus some particles can be missed. When the particle distributions are reconstructed from two successive frames, the missing particles may only be present in one frame rather than in the other frame, leading to the loss-of-pair particles. In PTV, these loss-of-pair particles affect the particle matching accuracy and reduce the measurement precision of the velocity field[49, 50]. A cross-validation matching (CVM) strategy (i.e., involves forward matching, backward matching and cross-validation of the two matching results) can be used to resolve this issue[49, 50]. This strategy reduces the impact of loss-of-pair particles on the matching accuracy effectively. It is anticipated that by integrating the CVM strategy into the hybrid PIV-PTV, the accuracy of the particle matching can be improved, and the measurement precision of the high-resolution velocity field can be enhanced.

In this study, a LF PIV-PTV along with a CVM is proposed for high-resolution microscale 3D velocity field measurement. First, the integration strategy of the hybrid PIV-PTV algorithm with CVM in LF-μPIV/PTV is explained. Second, numerical simulations are performed to reconstruct the 3D displacement field under higher particle stretching. The capability of the proposed method is assessed to achieve precise individual particle tracking at higher particle concentrations. The effects of the different parameters (such as interrogation window size, particle diameter and concentration) on the reconstruction performance are also carried out and subsequently facilitate the optimized parameters. Experimental evaluations of the proposed method are conducted on the microscale 3D velocity field measurement within the microchannel with right-angle bends. The results achieved from the simulations and experiments are presented and discussed.

2 Light field PIV-PTV

It is crucial to obtain the displacement field of tracer particles for the velocity field measurement, as the velocity field is measured by calculating the ratio of particle displacement field to the time interval between two consecutive frames. Thus, in this section, the displacement field instead of the velocity field is discussed.

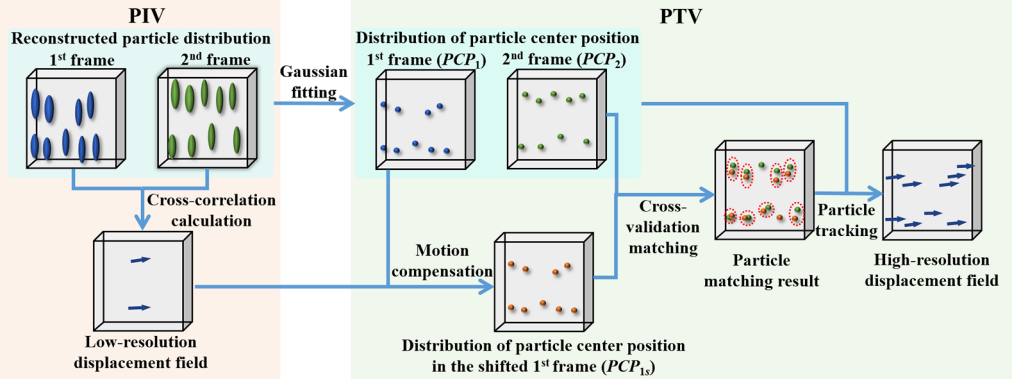

Fig. 1 Technical strategy of the LF PIV-PTV in combination with CVM.

Fig. 1 illustrates the principle of the LF PIV-PTV in combination with CVM. The low-resolution displacement field is achieved through CC calculation between the reconstructed particle distributions of two successive frames. The distributions of particle center position in the first (PCP_1) and second (PCP_2) frames are obtained by employing Gaussian fitting to the particle intensity values of each reconstructed particle, as the reconstructed particle intensity values correspond to the Gaussian distribution function[31]. To reduce the particle displacement and improve the matching accuracy, motion compensation is performed on the PCP_1 using the low-resolution velocity field. As a result, PCP_1 is adjusted to the distribution of particle center position in the shifted first frame (PCP_{1s}). Then the particle matching is performed between PCP_{1s} and PCP_2 through a nearest neighbor method based on the CVM. Once the particle matching is achieved, the proposed method is used to track individual particles thus providing the high-resolution displacement field measurement.

During the CC calculation, the measurement volume is divided into multiple interrogation windows. Then, the normalized CC coefficient R is calculated for each interrogation window and defined as[51]

$$R(l,m,n)=\frac{\sum_{i,j,k=1}^{I,J,K}E_1(i,j,k)\times E_2(i-l,j-m,k-n)}{\sqrt{\sum_{i,j,k=1}^{I,J,K}E_1(i,j,k)^2\times\sum_{i,j,k=1}^{I,J,K}E_2(i,j,k)^2}}, \tag{1}$$

where E_1 and E_2 denote the intensity distribution of the reconstructed particles within the interrogation window of the first and second frames, respectively. (I, J, K) denotes the total voxel numbers in the x, y and z-directions, (i,j,k) is the control variable and (l,m,n) denotes the 3D displacement in voxels. R is from -1 to 1 and a large R corresponds to a higher correlation. The average particle displacement within the interrogation window is estimated as the peak position of the CC coefficient, where the maximum R is located. Once the average particle displacements for all interrogation windows are determined, the low-resolution displacement field of the tracer particles can be obtained.

After CC calculation, the low-resolution displacement field is used for motion compensation in the hybrid PIV-PTV method, which transforms PCP_1 to PCP_{1s}. This can be expressed as

$$\begin{bmatrix} c_{1s,x} \\ c_{1s,y} \\ c_{1s,z} \end{bmatrix} = \begin{bmatrix} c_{1,x} \\ c_{1,y} \\ c_{1,z} \end{bmatrix} + \begin{bmatrix} dis_{c_1,x} \\ dis_{c_1,y} \\ dis_{c_1,z} \end{bmatrix}, \tag{2}$$

where c_1 and c_{1s} represent the particle center positions of PCP_1 and PCP_{1s}, respectively. dis_{c_1} represents the average particle displacement within the interrogation window where c_1 is located. Subscripts x, y and z represent 3D directions.

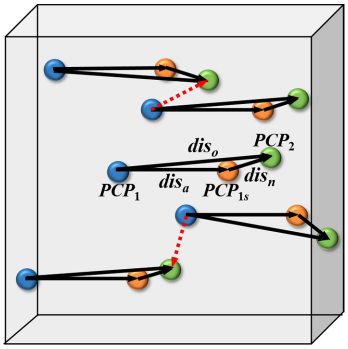

Fig. 2 Schematic diagram of the relationship between the particle displacements (illustrated in a single interrogation window)

As motion compensation transforms PCP_1 to PCP_{1s}, the particle matching using the nearest neighbor method is performed between PCP_{1s} and PCP_2 rather than between PCP_1 and PCP_2. This changes the particle displacement between two frames during the matching and affects the particle matching accuracy. Fig. 2 illustrates the relationship between the particle displacements before and after the motion compensation within a single interrogation window. The original displacement, dis_o is the particle displacement between PCP_1 and PCP_2 before motion compensation, whereas the new displacement, dis_n is the particle displacement between PCP_{1s} and PCP_2 after motion compensation. Additionally, the average displacement, dis_a is the particle displacement between PCP_1 and PCP_{1s}. As shown in Fig. 2, the dis_o, dis_n and dis_a together formed a vector triangle, which implies that dis_n is the vector difference between the dis_o and dis_a (i.e., $dis_n = dis_o - dis_a$). Generally, the dis_a obtained by CC calculation approaches to dis_o[33] and leads to a significantly smaller value of dis_n compared to dis_o. For the nearest neighbor method, a small particle displacement indicates a high particle matching accuracy[38, 42]. For example, when conducting the particle matching between PCP_{1s} and PCP_2, a smaller dis_n ensures that no additional particles are visible within the range of particle displacement, thus forming accurate matching pairs. However, when performing particle matching between PCP_1 and PCP_2, a larger dis_o will lead to the presence of other particles within the displacement range, resulting in the invalid matching pairs, i.e., incorrect displacements, as illustrated by the red dashed lines in Fig. 2. Consequently, the hybrid PIV-PTV method improves the particle matching accuracy through motion compensation.

However, it should be noted that the dis_a is obtained by the CC calculation and affected by multiple parameters such

as interrogation window size, particle diameter and concentration[33]. When these parameters are not properly optimized, a large deviation arises between the dis_a and dis_o, leading to fault motion compensation. As a result, the particles in the first frame may be shifted to incorrect positions, thereby affecting the particle matching accuracy.

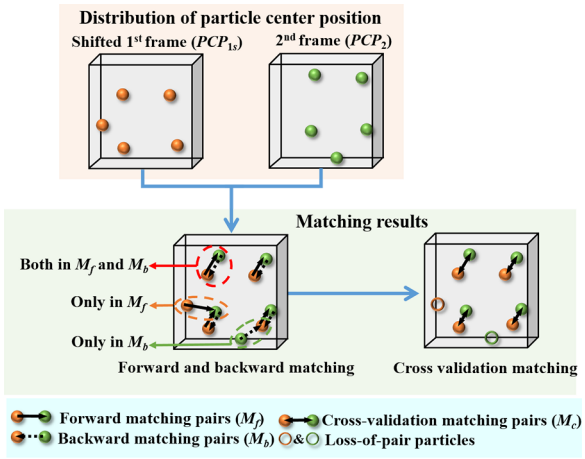

Fig. 3 Principle of the nearest neighbor method based on CVM.

Although the hybrid PIV-PTV algorithm improves the matching accuracy through the nearest neighbor method based on motion compensation, the presence of loss-of-pair particles still generates invalid matching pairs and reduces the measurement precision. To mitigate the impact of loss-of-pair particles, the CVM strategy[49, 50] is introduced. Fig. 3 shows the principle of the nearest neighbor method based on the CVM. This method involves the forward ($PCP_{1s} \rightarrow PCP_2$), backward ($PCP_2 \rightarrow PCP_{1s}$) matching and cross-validation of two matching pairs. In forward matching, a single particle in PCP_{1s} forms a forward matching pair with the particle in PCP_2 through the nearest neighbor method. Similarly, in the backward matching, a single particle in PCP_2 forms a backward matching pair with the particle in PCP_{1s} through the nearest neighbor method. The cross-validation is then performed on the forward and backward matching pairs, which is expressed as

$$\boldsymbol{M}_c = \boldsymbol{M}_f \cap \boldsymbol{M}_b, \tag{3}$$

where $\boldsymbol{M_c}$, $\boldsymbol{M_f}$ and $\boldsymbol{M_b}$ denote the cross-validation, forward matching, and backward matching pairs, respectively. The symbol "∩" denotes the intersection operation. The CVM reduces the invalid matching pairs generated by loss-of-pair particles, as illustrated by the orange and green dashed circles in Fig. 3. Consequently, the impact of loss-of-pair particles on particle matching has significantly diminished. Finally, substituting $\boldsymbol{M_c}$ into PCP_1 and PCP_2 for particle tracking, the LF PIV-PTV along with CVM enables the high-resolution displacement field measurement.

3 Numerical study

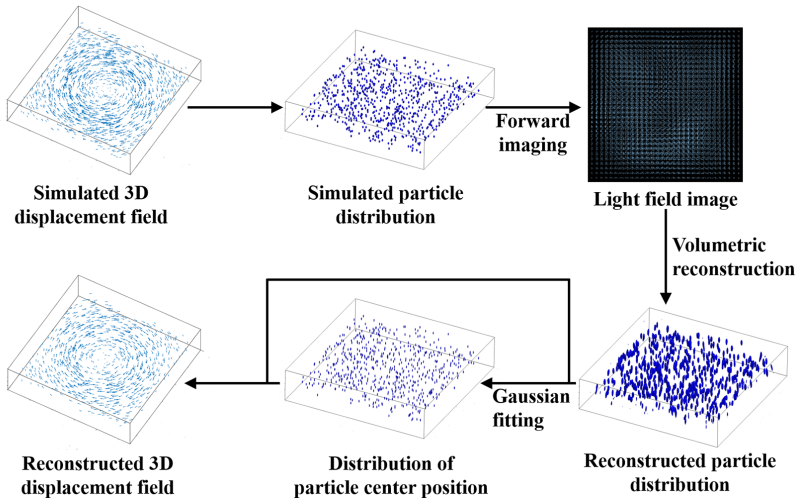

Fig. 4 Simulation process for the reconstruction of 3D displacement field of tracer particles

Once the time interval between two successive frames of LF images is established, the velocity and displacement field can mutually be transformed. Moreover, the precision of the displacement field is solely influenced by the CC calculation or particle matching algorithm and is independent of the time interval. Therefore, numerical simulation is conducted to reconstruct the 3D displacement field of tracer particles and to investigate the effects of the interrogation window size, particle diameter and particle concentration. Fig. 4 illustrates the simulation process of the reconstruction of the 3D displacement field. Initially, two frames of simulated particle distributions are generated within the measurement volume according to the simulated 3D displacement field of tracer particles. Forward imaging is performed based on the optical parameters of the LF microscope (Table 1) to obtain the LF images[48, 52]. The LF images are then used to reconstruct the particle distributions using the low-rank decomposition-based deconvolution (LRDD) algorithm[31], despite encountering a larger reconstructed particle stretching. Subsequently, Gaussian fitting is applied to the reconstructed particle distributions to obtain the corresponding distributions of the particle center position. Finally, the reconstructed particle distributions and the distributions of particle center position are then used to achieve the reconstruction of the 3D displacement field of tracer particles by the proposed method.

The optical parameters used in the simulation are listed in Table 1. The size of the measurement volume is set to 220×220×50 μm^3, with a discrete voxel size of 0.275×0.275×2 μm^3. To minimize the stretching of the reconstructed particles, the center of measurement volume is positioned at a distance of 45 μm from the focal plane of the LF microscope[35], and thus mitigates the effect of the depth location of measurement volume on the low-resolution displacement field of PIV[33].

Table 1 Optical Parameters of LF Microscope

Elements	Parameters	Values
Objective lens	Magnification (M_m)	20
	Numerical aperture (NA)	0.5
Microlens array	Microlens pitch (D)	150 μm
	Focal length (f_μ)	3000 μm
Camera	Pixel pitch (P_p)	5.5 μm

The simulated particle distribution in the first frame is randomly generated, whereas the second frame is formed by shifting the particles in the first frame according to the simulated 3D displacement field of tracer particles. The simulated 3D displacement field of tracer particles is the Rankine vortex[53] with different displacements at varying depths, which can be expressed as

$$D(r,z)=\begin{cases} D_{\max}\dfrac{r}{R}\left(1-\dfrac{|z-z_c|}{z_{\max}-z_c}\right), & 0\le r\le R \\ D_{\max}\dfrac{R}{r}\left(1-\dfrac{|z-z_c|}{z_{\max}-z_c}\right), & \mathrm{r>R} \end{cases} \quad \text{with } r=\sqrt{(x-x_c)^2+(y-y_c)^2}, \tag{4}$$

where $D(r, z)$ denotes the displacement at the location (r, z), (x_c, y_c, z_c) denotes the center of the measurement volume. $z_{\max}$ denotes the maximum depth of the measurement volume, which is 50 μm. $D_{\max}$ denotes the maximum displacement of the vortex and is set to 11 μm, and R denotes the radius of the vortex and is set to 110 μm. The simulated 3D displacement field of tracer particles at a concentration of 1.5 ppm is shown in Fig.4.

In the simulated particle distribution, the intensity distribution of each particle is modeled by a 3D Gaussian function, which is expressed as

$$I(x,y,z)=\exp\left\{-\frac{8\left[(x-x_p)^2+(y-y_p)^2+(z-z_p)^2\right]}{d_p^2}\right\}, \tag{5}$$

where $I(x, y, z)$ represents the intensity of a single particle at the location (x, y, z), (x_p, y_p, z_p) represents the center of the

particle and d_p represents the particle diameter. Notably, the particle concentration and diameter can be adjusted to suit different simulated conditions.

To evaluate the performance of the reconstructed 3D displacement fields through the proposed method, vector spacing (s_{vec}) and displacement error (ε_{dis}) are introduced as performance metrics. The s_{vec} is utilized to evaluate the spatial resolution of the reconstructed 3D displacement field, which is expressed as,

$$s_{vec} = \sqrt[3]{\frac{3V_m}{4\pi N_{vec}}}, \tag{6}$$

where V_m is the measurement volume (in μm^3), and N_{vec} is the number of independent displacement vectors. Since the size of the measurement volume is fixed, the vector spacing depends on the number of displacement vectors. A small s_{vec} indicates the high spatial resolution of the reconstructed 3D displacement field.

The displacement error, ε_{dis}, is used to evaluate the precision of the reconstructed displacement field, which is defined as

$$\varepsilon_{dis} = \sqrt{\frac{1}{N_{vec}} \sum_{i=1}^{N_{vec}} \left(d_{mea,i} - d_{truth,i} \right)^2}, \tag{7}$$

where $d_{mea,i}$ and $d_{truth,i}$ are the measured value and true value of the i_{th} displacement vector, respectively. A small ε_{dis} indicates the high precision of the reconstructed 3D displacement field.

Furthermore, the 3D displacement fields are also reconstructed through the PIV, PTV and PIV-PTV methods, and their performance is compared with the proposed method. Notably, when the vector spacing in Eq. (6) is employed to assess the spatial resolution, the number of independent velocity vectors (N_{vec}) is determined by the number of matched particle pairs within the measurement volume for the PTV, PIV-PTV and the proposed method. Conversely, in PIV, N_{vec} is equal to the number of non-overlapping interrogation windows within the measurement volume[54].

3.1 Influence of interrogation window size

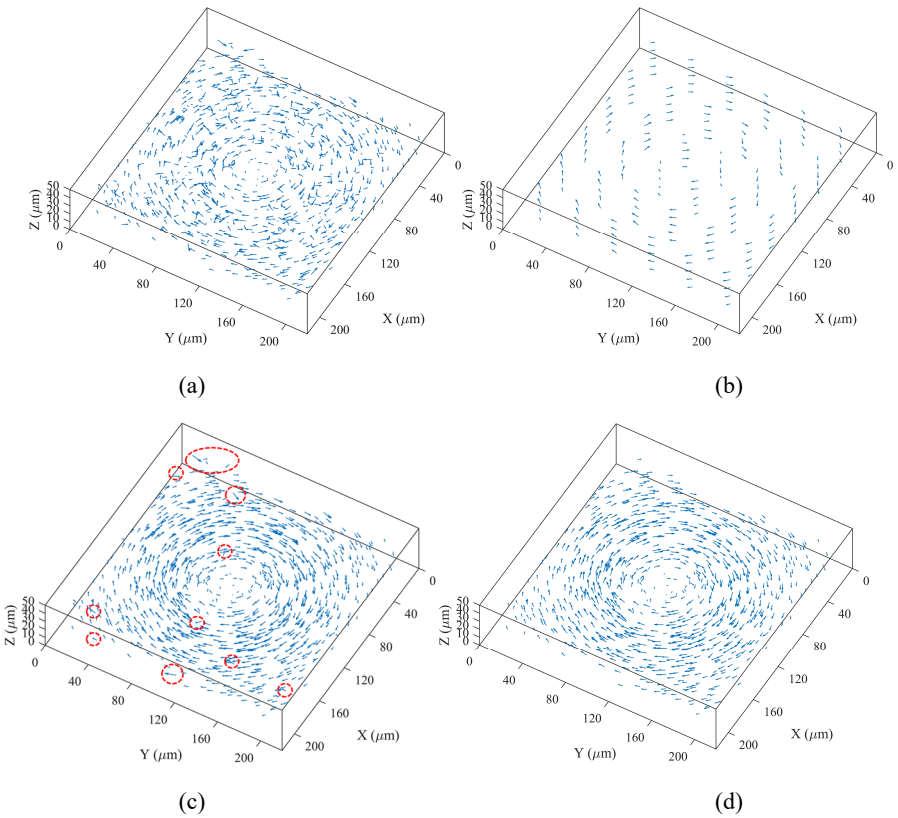

Fig. 5 Comparison of the reconstructed 3D displacement fields: (a)PTV, (b)PIV, (c) PIV-PTV and (d) Proposed method.

Fig. 5 depicts the reconstructed 3D displacement fields achieved by the PTV, PIV, PIV-PTV and the proposed

method. The particle diameter and concentration are set to 2 μm and 1.5 ppm, respectively. An interrogation window with the size of 128×128×6 voxels is applied. Compared to the simulated 3D displacement field in Fig. 4, it can be observed that though PTV provides high spatial resolution, it is plagued with numerous incorrect vectors violating the vortex structure, thus providing lower precision. Conversely, the PIV correctly reveals the structure of the Rankine vortex and provides a higher precision than the PTV, but its displacement vectors are sparse, resulting in lower spatial resolution. However, the PIV-PTV and the proposed method both exhibit higher spatial resolution and precision. Furthermore, the proposed method reduces the incorrect vectors generated by the loss-of-pair particles [as shown by the red dashed line in Fig. 5(c)] through the CVM. Therefore, it is demonstrated that the proposed method overcomes the low spatial resolution of the PIV and low precision of the PTV under higher particle concentrations and mitigates the impact of loss-of-pair particles, thus achieving a high-precision and high-resolution reconstruction of the 3D displacement field.

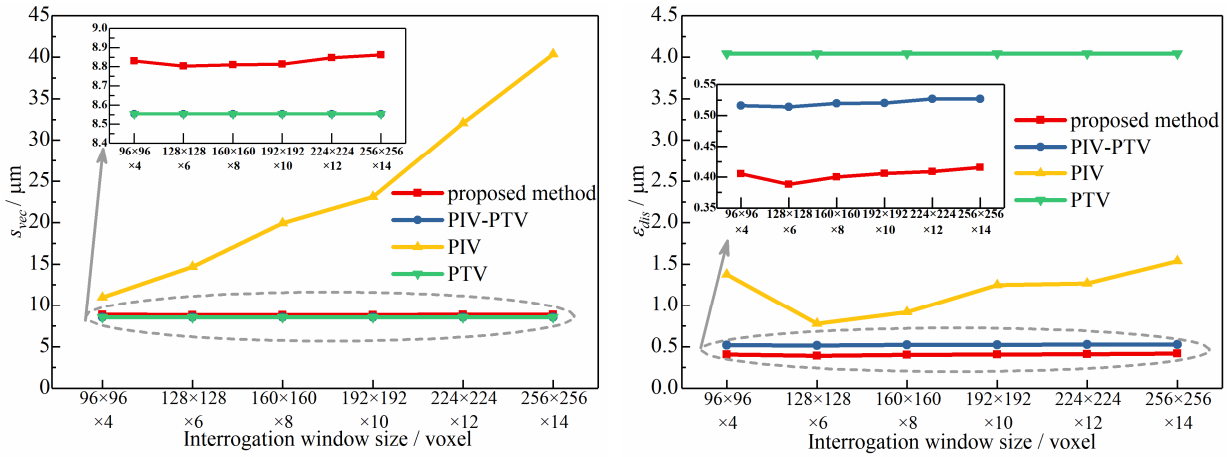

Fig. 6 Performance of reconstructed 3D displacement field under different interrogation window sizes: (a) Vector spacing and (b) Displacement error.

Fig. 6 illustrates the influence of the interrogation window size on vector spacing and displacement error of the reconstructed 3D displacement fields achieved by the PTV, PIV, PIV-PTV and the proposed method. As shown in Fig. 6(a), under different interrogation window sizes, the PIV always yields larger vector spacing than the PTV, PIV-PTV and the proposed method. This is attributed to the fact that PIV requires multiple particles to compute a single reliable displacement vector through CC calculation. While PTV, PIV-PTV and the proposed method can track an individual particle to obtain a displacement vector. The vector spacing of PTV and PIV-PTV is the same but slightly smaller than that of the proposed method. Because the PTV and PIV-PTV only perform forward matching, while the proposed method employs CVM, which reduces the number of invalid matching pairs and thus leads to increased vector spacing. Moreover, increasing the interrogation window size decreases the number of non-overlapping interrogation windows within the measurement volume (i.e., N_{vec} in PIV). Thus, the vector spacing of PIV constantly increases with the interrogation window sizes. For PTV, PIV-PTV and the proposed method, the vector spacings depend on the number of matching pairs within the measurement volume and are independent of the interrogation window size. However, the vector spacing of the proposed method initially decreases and then increases with the interrogation window size due to the displacement error, which is discussed in the following paragraphs.

In Fig. 6(b), it can be observed that the displacement error of the proposed method is smaller than the PTV, PIV and PIV-PTV across varying interrogation window sizes. This evidence supports that the proposed method can improve the precision of the reconstructed 3D displacement field. As the interrogation window size increases, the displacement error of PIV decreases initially and then increases, reaching a minimum at the interrogation window size of 128×128×6 voxels. This can be attributed to the fact that, at a constant particle concentration, the interrogation window size determines the number of particles within the window, influencing the precision of the reconstructed 3D displacement field of PIV. For an interrogation window size of 96×96×4 voxels, only 2 particles are present within the window, which is insufficient for the CC calculation and increases the displacement error of PIV[55]. However, increasing the interrogation window size

to 128×128×6 voxels causes 5 particles to appear within the window, which satisfies the requirement of the CC calculation, thus reducing the displacement error of PIV. Further increasing the interrogation window size enhances the spatial filtering effect and increases the displacement error of PIV[55]. Thus, to ensure the precision of PIV, the interrogation window should strike a balance: it must be sufficiently large to avoid inadequate particle data for the CC calculation, yet not excessively large to avoid expanding spatial filtering effects. A small interrogation window, containing at least 4 particles is recommended to achieve the minimum displacement error for PIV.

It should be noted that the displacement error of PIV [in Fig. 6(b)] is from 0.77 to 1.54 μm, which is equivalent to 3 to 6 voxels. In this scenario, some particles in the PCP_{1s} formed by motion compensation are shifted to incorrect positions due to the displacement error of PIV, leading to invalid matching pairs during the particle matching between the PCP_{1s} and PCP_2. As the displacement error of PIV increases, the number of invalid matching pairs also increases. Therefore, the displacement error of PIV-PTV and the proposed method shows a consistent trend with that of PIV as the interrogation window size increases. However, some invalid matching pairs are reduced through the CVM, thus increasing the vector spacing. In addition, a larger displacement error of PIV leads to a substantial increment of vector spacing. Consequently, like the variation of displacement error of PIV with interrogation window size, the vector spacing of the proposed method decreases and then increases with increasing interrogation window size as depicted in Fig. 6(a). It is, therefore, suggested that a small interrogation window containing at least 4 particles should be selected to improve the spatial resolution and precision of the reconstructed 3D displacement field.

3.3 Influence of particle diameter

Fig. 7 presents a comparative analysis of the performance of reconstructed 3D displacement fields achieved by the PTV, PIV, PIV-PTV and the proposed method for different diameters of tracer particles. As illustrated in Fig. 7(a), the vector spacing of PIV remains constant with increasing particle diameter due to the fixed interrogation window size. For PTV, PIV-PTV and the proposed method, the vector spacings show slight variation under different particle diameters. This is due to the consistent particle missing rates under different particle diameters, as shown in Fig. 8(a). The particle missing rate represents the ratio of recognized reconstructed particles to the simulated particles. Increasing the particle diameter modifies the voxel intensity values and stretches the reconstructed particle further[33]. However, the voxel intensity values of reconstructed particles still follow a Gaussian distribution and can be recognized through the Gaussian fitting. Consequently, the variation in particle missing rates under different particle diameters remains below 0.5%. This suggests that changing the particle diameter has no significant impact on the number of recognized reconstructed particles as well as the vector spacing.

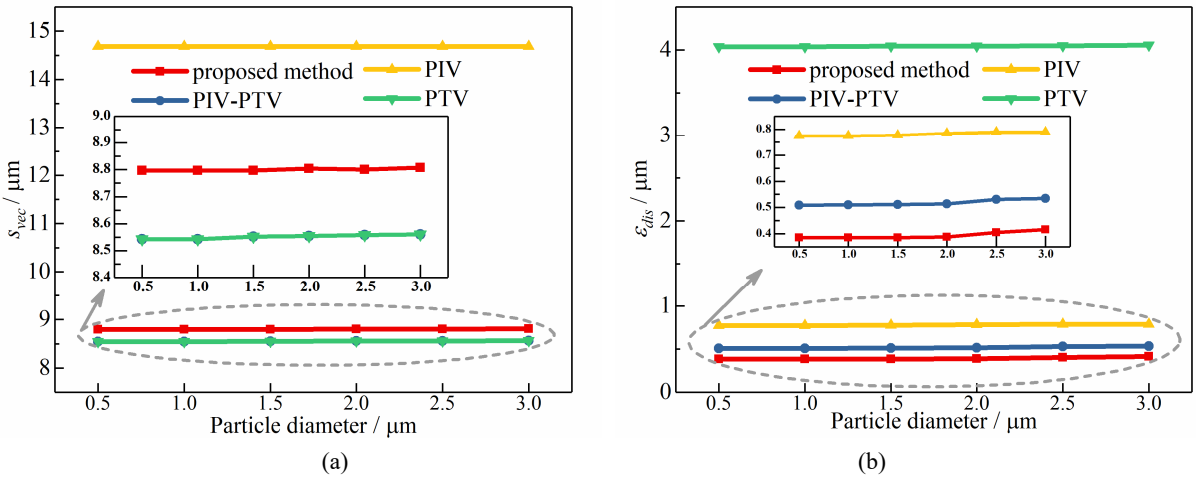

Fig. 7 Performance of reconstructed 3D displacement field under different particle diameters: (a) Vector spacing and (b) Displacement error.

In Fig. 7(b), it can be seen that the displacement error of PIV slightly increases with the increment of particle diameter, which is due to the stretching effect of larger particles[33]. However, the impact of particle diameter on the

displacement error of PIV is limited. For instance, as the particle diameter increases from 0.5 μm to 3 μm, the displacement error of PIV increases from 0.77 μm to 0.79 μm. The change in displacement error of PIV is less than 0.1 voxel, indicating a consistent effect on motion compensation. That means the displacement error of the proposed method remains unchanged across different particle diameters. However, a notable increment of displacement error is achieved by the proposed method when the particle diameter exceeds 2 μm. This is attributed to the fact that the displacement error is also affected by the error of particle center position[46]. The determination of the particle center position relies on identifying the peak position of the Gaussian fitting function. When the particle diameter exceeds 2 μm, the stretching is significantly increased and the voxel intensity value changes extensively. As a result, a shift in the peak position of the Gaussian function can be observed and the error of particle center position is increased, as shown in Fig. 8(b). Consequently, the proposed method also shows an increment in the displacement error when the particle diameter exceeds 2 μm. Therefore, the particle diameters should not exceed 2 μm to reduce the impact of error of the particle center position and improve the precision of the proposed method.

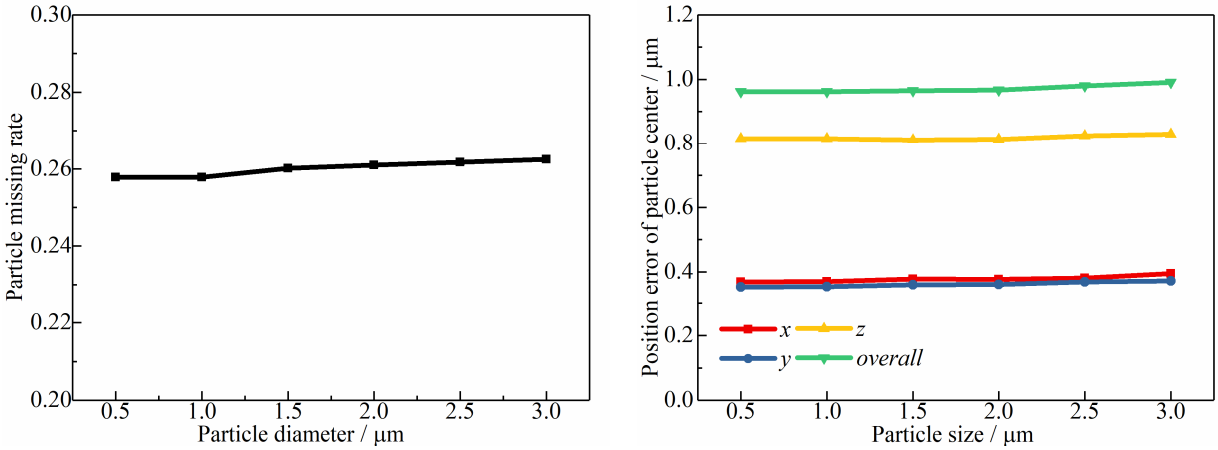

Fig. 8 Quality of reconstructed particle distribution: (a) Particle missing rate and (b) Position error of particle center

3.4 Influence of particle concentration

As observed in Section 3.2, the number of particles is determined by the particle concentration and the interrogation window. It is also suggested that a smaller interrogation window containing no fewer than 4 particles should be selected. Thus, an appropriate window size should be determined based on the particle concentration. Table 2 presents the particle concentrations and corresponding window sizes chosen for this investigation. In addition, the particle diameter is set as 2 μm according to Section 3.3. Fig. 9 depicts the vector spacing and displacement errors of the reconstructed 3D displacement field achieved by the PTV, PIV, PIV-PTV and the proposed method at different particle concentrations. It can be observed [Fig. 9(a)] that the vector spacing decreases with increasing particle concentration. For PTV, PIV-PTV and the proposed method, increasing the particle concentration increases the number of particle matching pairs within the measurement volume, leading to a reduction of vector spacing. For PIV, increasing particle concentration results in a higher number of displacement vectors since the interrogation window size for CC calculation decreases (refer to Table 2). Consequently, this leads to a step-like decrease in the vector spacing. However, to obtain accurate displacement vectors in PIV, multiple particles are always necessary, and this creates a larger vector spacing than the PTV, PIV-PTV and the proposed method.

Table 2 Interrogation window sizes for different particle concentrations

Particle concentration/ppm	0.30	0.45	0.60-0.90	1.05-1.95
Interrogation window size/voxel	224×224×12	192×192×10	160×160×8	128×128×6

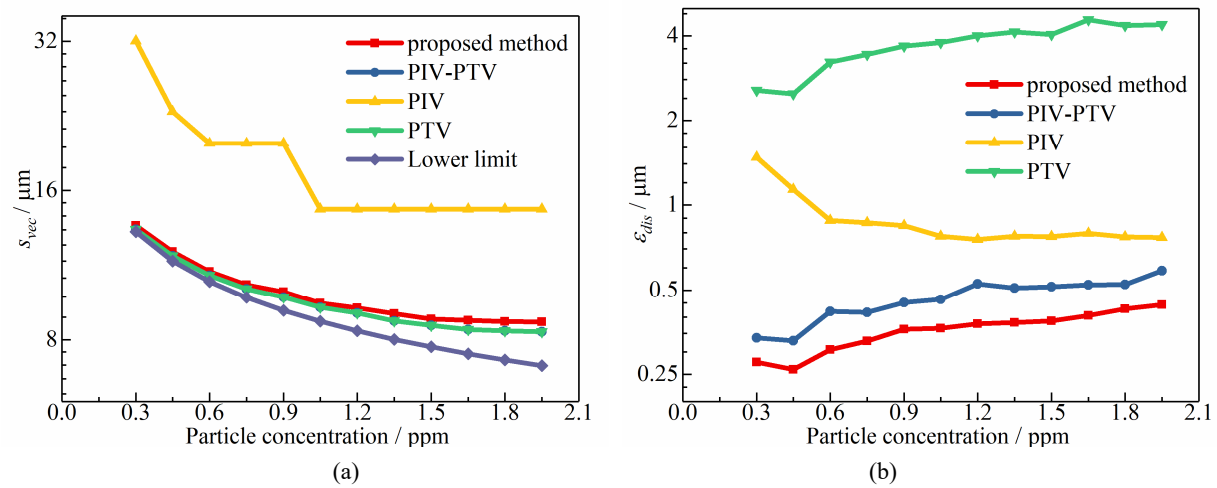

Fig. 9 Performance of reconstructed 3D displacement field under varying particle concentrations: (a) Vector spacing and (b) Displacement error.

Notably, the number of simulated particles within the measurement volume determines the lower limit of the vector spacing for the reconstruction of the 3D displacement field, as indicated by the purple curve in Fig. 9(a). However, for the proposed method, as the particle concentration increases, the gap between the reconstructed vector spacing and the lower limit progressively widens due to the increased particle missing rate, as shown in Fig. 10(a). A higher particle concentration creates more overlap between the reconstructed particles, thereby affecting the accuracy of identifying the particle center position through the Gaussian fitting. Increasing the particle concentration consequently increases the difference between the number of recognized reconstructed particles and the simulated particles, resulting in a wider gap between the reconstructed vector spacing and the lower limit. Moreover, as the particle concentration increases from 1.5 ppm to 1.95 ppm, the particle missing rate escalates from 0.26 to 0.38. This increases a higher number of loss-of-pair particles. However, the CVM reduces the invalid displacement vectors caused by the loss-of-pair particles. As a result, the increase in the number of displacement vectors becomes tardily once the particle concentration surpasses 1.5 ppm. This indicates that in the proposed method, the vector spacing reaches a saturation point at a particle concentration of 1.5 ppm due to the deteriorated particle reconstruction quality.

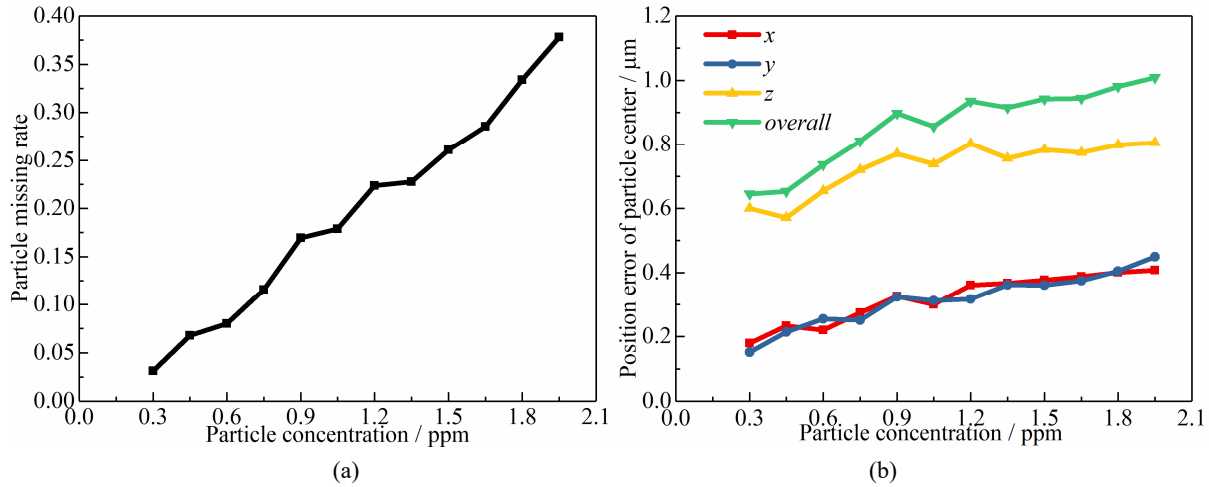

Fig. 10 Quality of reconstructed particle distribution at different particle concentrations: (a) Particle missing rate and (b) Position error of particle center.

Fig. 9(b) depicts the variation of displacement errors achieved by the PTV, PIV, PIV-PTV and the proposed method with different particle concentrations. For PIV, the displacement error reduces significantly with increasing particle concentration. This is due to the reduction of interrogation window size as shown in Table 2, which in turn decreases the spatial filtering effect of the CC calculation[55]. Specifically, as the particle concentration increases from 0.3 ppm to 1.95

ppm, the displacement error decreases from 1.48 μm (approximately 5 voxels) to 0.77 μm (approximately 3 voxels). For the proposed method, increasing the particle concentration increases the displacement error. This is because the error of the reconstructed particle center position affects the displacement error. A higher particle concentration increases the particle overlapping and shifts the peak position of the Gaussian fitting function. Consequently, the error of particle center position increases with particle concentration as shown in Fig. 10(b), thereby exacerbating the displacement error. However, by employing the motion compensation and CVM, the proposed method provides minimum displacement error under different particle concentrations compared to other methods.

4 Experimental validations

To validate the proposed method, experiments were conducted on a microscale 3D velocity field within the microchannel with right-angle bends. The experimental setup illustrated in Fig. 11(a) consists of a LF microscope, a synchronizer and a microchannel with right-angle bends. The LF microscope is composed of an inverted microscope, a MLA and a CCD camera. The parameters listed in Table 1 are used for the LF microscope. The synchronizer is used to ensure synchronized control of the laser and the camera. The tracer particle is fluorescent polystyrene microspheres with a diameter of 2 μm and a density of 1.05 g/cm^3. During the experiment, the water injected into the microchannel is seeded with tracer particles at a concentration of 1.5 ppm. The measurement volume, located in the right-angle bend region as shown in Fig. 11(b), has a size of 240 × 280 × 50 μm^3 (L×W×H) and is discretized into voxels with the size of 0.275 × 0.275 × 2 μm^3. The microchannel in this region has a depth of 50 μm and widths of 220 μm and 500 μm on either side of the right-angle bend. The raw LF image of tracer particles, reconstructed particle distribution and the distribution of particle center position are shown in Fig. 12.

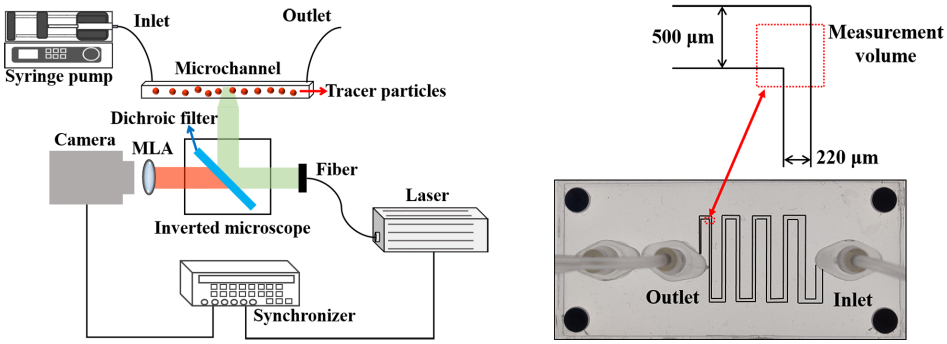

(a) (b)

Fig. 11 Schematic diagram of the experimental setup: (a) LF PIV-PTV System and (b) Microchannel.

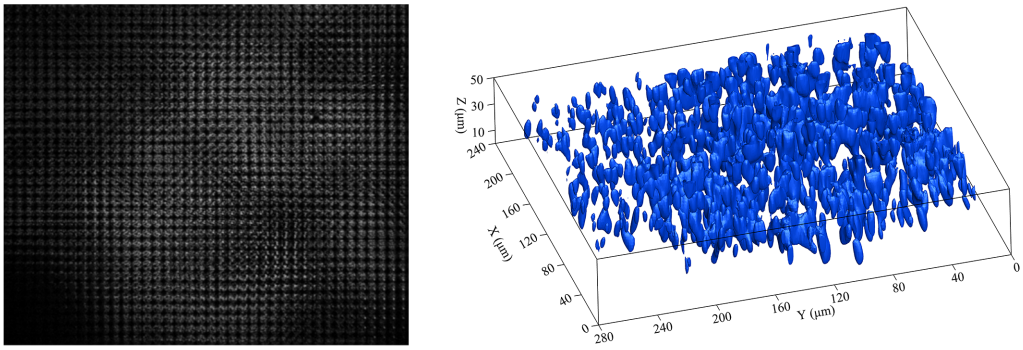

(a) (b)

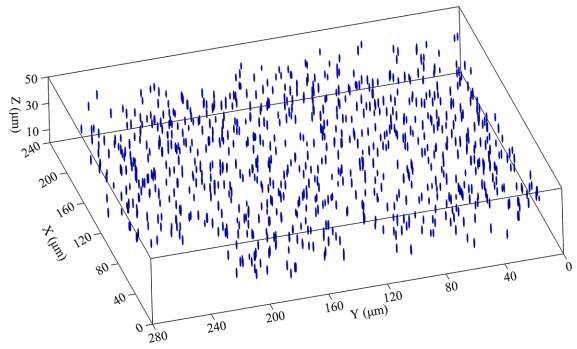

(c)

Fig. 12 An example of (a) Raw LF image, (b) Reconstructed particle distribution and (c) Distribution of particle center position.

The experimental velocity fields obtained by the PTV, PIV, PIV-PTV and the proposed method at an inlet flow rate of 9 μL/min are shown in Fig. 13. The interrogation window size used in the CC calculation is 128×128×6 voxels. To verify the accuracy of the experimental velocity fields, a theoretical velocity field is also achieved through computational fluid dynamics (CFD) based on the laminar flow model[30], as shown in Fig. 14. The flow structure obtained through PTV does not resemble accurately the theoretical velocity field, suggesting a lower precision level. In contrast, the flow structures acquired by the PIV, PIV-PTV and the proposed method aligned with the theoretical velocity field. However, it can be observed that both the PIV-PTV and the proposed method provide more velocity vectors than the PIV by tracking individual particles. In addition, the proposed method utilizes the CVM for reducing approximately 40 erroneous vectors generated by the loss-of-pair particles in the PIV-PTV [red dashed circle in Fig. 13(c)], thereby further improving the precision of the velocity field.

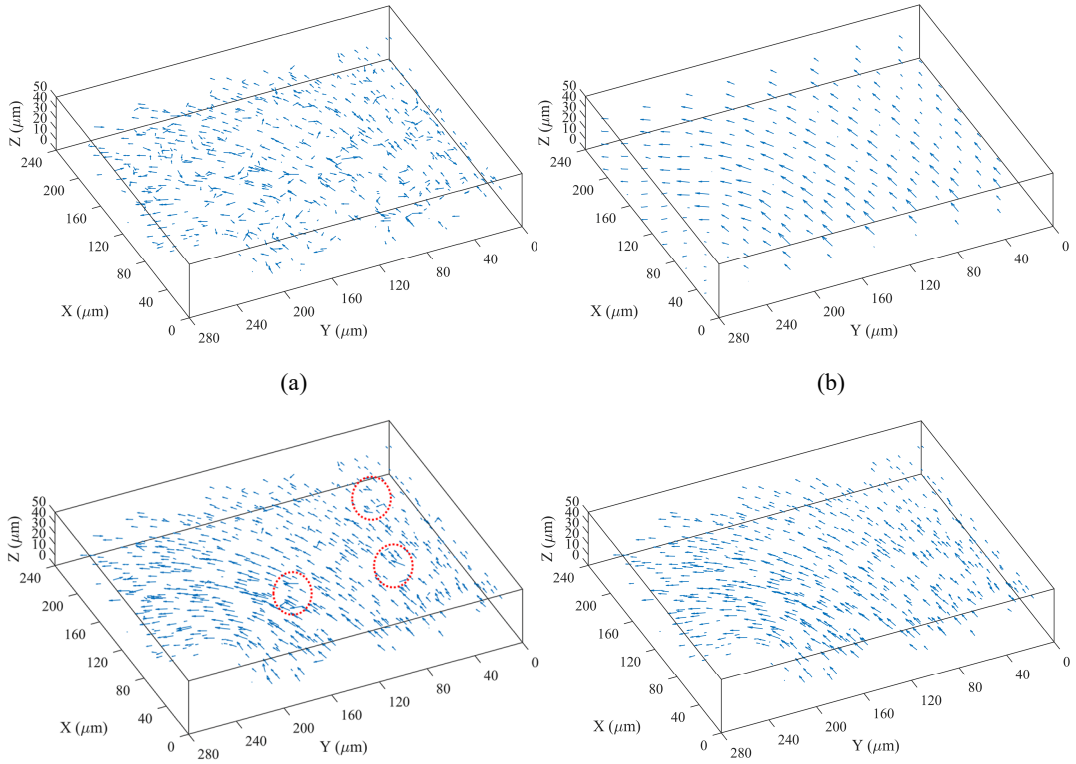

Fig. 13 Experimental velocity fields: (a) PTV; (b) PIV; (c) PIV-PTV and (d) Proposed method.

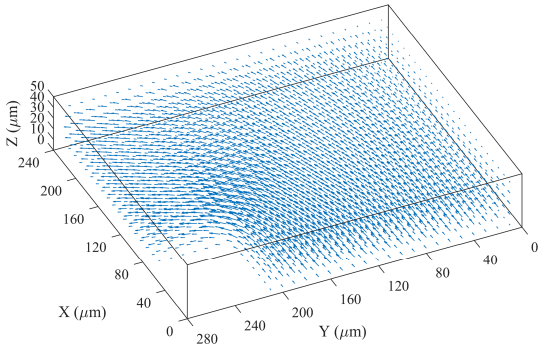

Fig. 14 Theoretical velocity field

Furthermore, the vector spacing and velocity error of different experimental velocity fields are compared. The vector spacing is obtained using Eq. (6). The velocity error, denoted by ε_{vel}, is defined as

$$\varepsilon_{vel} = \sqrt{\frac{1}{N_{vel}} \sum_{i=1}^{N_{vel}} \left(v_{exp,i} - v_{theory,i} \right)^2}, \tag{8}$$

where $v_{exp,i}$ and $v_{theory,i}$ represent the experimental and theoretical values of the i_{th} velocity vector, respectively, and N_{vel} is the total number of velocity vectors.

Fig. 15 illustrates the vector spacing and velocity error of the velocity field for PTV, PIV, PIV-PTV and the proposed method at different inlet flow rates. To assess the effect of time interval on the precision of the velocity field, the time interval of two consecutive frames is set to 500 μs, 500 μs and 250 μs for inlet flow rates of 5 μL/min, 9 μL/min, and 18 μL/min, respectively. As shown in Fig. 15(a), the vector spacing of PIV remains consistent with the results obtained by the simulation as depicted in Fig. 9, with a fixed value of 14.68 μm without deviation. This is achieved by maintaining a constant integration window size of 128×128×6 voxels. Similar vector spacings are achieved for the PTV and the PIV-PTV but slightly lower than the proposed method, which is also consistent with the simulation results (Fig. 9). This indicates that, under the experimental conditions, the proposed method can reduce the erroneous vectors caused by loss-of-pair particles through the CVM. Notably, the average vector spacing of 10.75 μm achieved by the proposed method is higher than the simulation vector spacing of 8.80 μm. This is due to the lack of an accurately identified number of reconstructed particles caused by calibration errors and image noises. Nevertheless, the vector spacing achieved by the proposed method is 26% lower than that of the PIV. It further demonstrates that the proposed method provides a higher spatial resolution for higher particle concentrations.

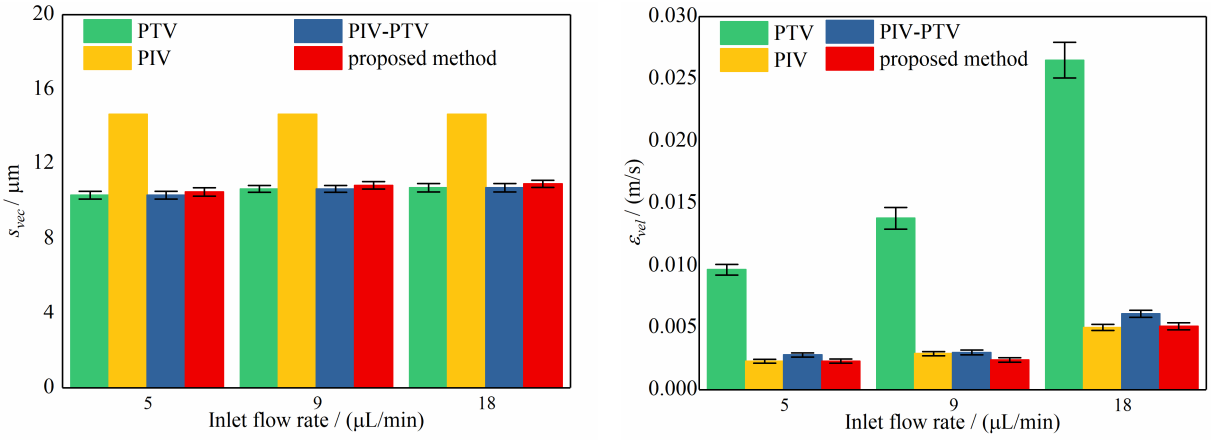

(a) (b)

Fig. 15 Velocity errors obtained at different inlet flow rates for different techniques: (a) Vector spacing and (b) Velocity error.

From Fig. 15(b), it can be observed that when the inlet flow rate increases from 5 μL/min to 9 μL/min, the velocity error achieved by the PTV increases significantly although the two-frame time interval is set to 500 μs. This is because

the increasing inlet flow rate leads to a larger particle displacement and decreases the particle matching accuracy for the PTV with the nearest neighbor method. When the inlet flow rate increases to 18 μL/min, the velocity errors increase significantly for the PTV, PIV, PIV-PTV and the proposed method due to the time interval of 250 μs, as the velocity errors are inversely proportional to the time interval[33]. Although velocity errors are affected by the inlet flow rates and two-frame time intervals for the different experimental conditions, the velocity error achieved for the proposed method is always lower compared to the PIV-PTV, which is consistent with the numerical simulation results (Fig. 9). However, the experimental velocity error achieved by the proposed method is like the PIV, which contradicts the simulation results where the proposed method has achieved significantly higher precision than the PIV. This can be explained by the fact that during the experiment, the position error of the particle center is exacerbated due to the calibration errors and image noise. Besides, the nearest neighbor method used in the proposed method is more sensitive to the position error of the particle center than the CC calculation used in the PIV[38]. Nevertheless, for the proposed method, the experimental velocity error is 76% lower than the PTV. Therefore, it demonstrates that the proposed method can overcome the shortcoming of lower precision achieved by the PTV at higher particle concentrations.

5 Conclusion

In this paper, a LF PIV-PTV along with cross-validation matching is proposed for high-resolution microscale 3D velocity field measurement. Numerical simulations were conducted for the 3D displacement fields of tracer particle reconstruction and investigated the influence factors such as the size of the interrogation window, particle diameter and particle concentration. Measurements of the microscale 3D velocity filed in a microchannel with right-angle bends were conducted to evaluate the performance of the proposed method. The concluding remarks drawn from this study are summarized as follows.

- The proposed method achieves individual particle tracking at higher particle concentrations and overcomes the shortcomings of low spatial resolution and precision involved in the PIV and PTV, also effectively reducing the erroneous vectors caused by loss-of-pair particles.
- It is suggested that a small interrogation window containing no fewer than 4 particles should be chosen during the cross-correlation calculation to improve the precision of the PIV, thereby improving the spatial resolution and precision of the proposed method. It is also suggested that the particle diameter should not exceed 2 μm to avoid a large position error of the particle center.
- The experimental study demonstrates that the proposed method can measure the high-resolution microscale 3D velocity fields accurately despite a slight reduction in the spatial resolution and precision compared to numerical simulation. At a particle concentration of 1.5 ppm, the proposed method outperforms the PIV and PTV by achieving a 26% improvement in spatial resolution and a 76% improvement in precision, respectively.

However, the proposed method cannot solve the loss of spatial resolution fully caused by particle missing during volumetric reconstruction. Future research focuses on optimizing the volumetric reconstruction process to reduce particle missing rates and improve the spatial resolution of the velocity field.

Acknowledgements

This study was supported by the National Natural Science Foundation of China (Nos. 51976038, 52006036), and Zhishan Scholarship of Southeast University (No. 2242022R40037).

Author declarations

Conflict of Interest

The authors have no conflicts to disclose.

Author Contributions

Mengtao Gu: Conceptualization (lead); Methodology (lead); Data curation (lead); Software (lead); Writing – original draft (lead). **Jian Li:** Data curation (supporting); Writing – review and editing (supporting); Funding acquisition

(supporting). **Md Moinul Hossain:** Writing – review and editing (lead). **Chuanlong Xu:** Supervision (lead); Funding acquisition (lead); Writing – review and editing (supporting).

Data Availability

The data that support the findings of this study are available from the corresponding author upon reasonable request.

References

1. Y. Liu, G. Yang, Y. Hui *et al.*, "Microfluidic nanoparticles for drug delivery," Small **18**, 2106580 (2022).
2. F. Tian, L. Cai, C. Liu *et al.*, "Microfluidic technologies for nanoparticle formation," Lab Chip **22**, 512 (2022).
3. L. Trabzon, G. Karimian, A. R Khosroshahi *et al.*, "High-throughput nanoscale liposome formation via electrohydrodynamic-based micromixer," Phys. Fluids **34**, (2022).
4. N. M. Pagán Pagán, Z. Zhang, T. V. Nguyen *et al.*, "Physicochemical characterization of asphaltenes using microfluidic analysis," Chem. Rev. **122**, 7205 (2022).
5. M. Yafia, O. Ymbern, A. O. Olanrewaju *et al.*, "Microfluidic chain reaction of structurally programmed capillary flow events," Nature **605**, 464 (2022).
6. Y. Gong, C. Zhang, X. Weng *et al.*, "Electrokinetically induced concentration of diluted sample by liquid metal embedded microfluidic chip," Phys. Fluids **34**, (2022).
7. J. Mohamed, M. Spizzichino, and G. P. Romano, "The effect of different carrier fluids on heat transfer performance in a microfluidic serpentine device," Int. J. Heat Mass Transfer **203**, 123788 (2023).
8. Y. Ye, B. Jiao, Y. Kong *et al.*, "Experimental investigations on the thermal superposition effect of multiple hotspots for embedded microfluidic cooling," Appl. Therm. Eng. **202**, 117849 (2022).
9. C. Keepaiboon, A. S. Dalkilic, O. Mahian *et al.*, "Two-phase flow boiling in a microfluidic channel at high mass flux," Phys. Fluids **32**, (2020).
10. A. Mariotti, C. Galletti, E. Brunazzi *et al.*, "Unsteady flow regimes in arrow-shaped micro-mixers with different tilting angles," Phys. Fluids **33**, 012008 (2021).
11. M. Nazari, S. Rashidi, and J. A. Esfahani, "Effects of flexibility of conductive plate on efficiency of an induced-charge electrokinetic micro-mixer under constant and time-varying electric fields-a comprehensive parametric study," Chem. Eng. Sci. **212**, 115335 (2020).
12. N. Burshtein, K. Zografos, A. Q. Shen *et al.*, "Periodic fluctuations of streamwise vortices in inertia-dominated intersecting flows," Phys. Fluids **33**, (2021).
13. R. M. Tona, T. A. McDonald, N. Akhavein *et al.*, "Microfluidic droplet liquid reactors for active pharmaceutical ingredient crystallization by diffusion controlled solvent extraction," Lab Chip **19**, 2127 (2019).
14. Y. Ding, P. D. Howes, and A. J. deMello, "Recent advances in droplet microfluidics," Anal. Chem. **92**, 132 (2019).
15. C. Chen, Z. Jing, C. Feng *et al.*, "Two-phase flow and morphology of the gas–liquid interface for bubbles or droplets in different microchannels," Phys. Fluids **35**, (2023).
16. C. Cierpka, and C. Kähler, "Particle imaging techniques for volumetric three-component (3D3C) velocity measurements in microfluidics," J. Vis. **15**, 1 (2012).
17. A. Etminan, Y. S. Muzychka, K. Pope *et al.*, "Flow visualization: state-of-the-art development of micro-particle image velocimetry," Meas. Sci. Technol. **33**, 092002 (2022).
18. J. S. Park, C. K. Choi, and K. D. Kihm, "Optically sliced micro-PIV using confocal laser scanning microscopy (CLSM)," Exp. Fluids **37**, 105 (2004).
19. M. Oishi, H. Kinoshita, T. Fujii *et al.*, "Simultaneous measurement of internal and surrounding flows of a moving droplet using multicolour confocal micro-particle image velocimetry (micro-PIV)," Meas. Sci. Technol. **22**, 105401 (2011).
20. J. Sheng, E. Malkiel, and J. Katz, "Digital holographic microscope for measuring three-dimensional particle distributions and motions," Appl. Opt. **45**, 3893 (2006).
21. T. Ooms, R. Lindken, and J. Westerweel, "Digital holographic microscopy applied to measurement of a flow in a T-shaped micromixer," Exp. Fluids **47**, 941 (2009).

22. R. Lindken, J. Westerweel, and B. Wieneke, "Stereoscopic micro particle image velocimetry," Exp. Fluids **41**, 161 (2006).
23. J. Giardino, J. Hertzberg, and E. Bradley, "A calibration procedure for millimeter-scale stereomicroscopic particle image velocimetry," Exp. Fluids **45**, 1037 (2008).
24. S. Y. Yoon, and K. C. Kim, "3D particle position and 3D velocity field measurement in a microvolume via the defocusing concept," Meas. Sci. Technol. **17**, 2897 (2006).
25. F. Pereira, J. Lu, E. Castano-Graff *et al.*, "Microscale 3D flow mapping with μDDPIV," Exp. Fluids **42**, 589 (2007).
26. Q. He, C. Willman, R. Stone *et al.*, "Inexpensive multi-plane particle image velocimetry based on defocusing: Proof of concept on two-component measurement," Phys. Fluids **35**, (2023).
27. T. T. Truscott, J. Belden, R. Ni *et al.*, "Three-dimensional microscopic light field particle image velocimetry," Exp. Fluids **58**, 16 (2017).
28. X. Song, M. Gu, L. Cao *et al.*, "A microparticle image velocimetry based on light field imaging," IEEE Sens. J. **19**, 9806 (2019).
29. M. Levoy, R. Ng, A. Adams *et al.*, "Light field microscopy," ACM Transactions on Graphics (TOG) **25**, 924 (2006).
30. M. Gu, J. Li, and C. Xu, "A modified Richardson–Lucy deconvolution for rapid reconstruction of light field μPIV," Exp. Fluids **63**, 59 (2022).
31. M. Gu, C. Xu, M. M. Hossain *et al.*, "A low-rank decomposition-based deconvolution algorithm for rapid volumetric reconstruction of light field μPIV," Exp. Fluids **64**, 39 (2023).
32. J. Westerweel, "Fundamentals of digital particle image velocimetry," Meas. Sci. Technol. **8**, 1379 (1997).
33. X. Zhu, C. Xu, M. M. Hossain *et al.*, "Approach to select optimal cross-correlation parameters for light field particle image velocimetry," Phys. Fluids **34**, 073601 (2022).
34. S. Shi, J. Wang, J. Ding *et al.*, "Parametric study on light field volumetric particle image velocimetry," Flow. Meas. Instrum. **49**, 70 (2016).
35. X. Song, J. Li, M. Gu *et al.*, "Parameters optimization of light field micro-particle image velocimetry," Opt. Commun. **475**, 126302 (2020).
36. S. Klein, J. Moran, D. Frakes *et al.*, "Three-dimensional three-component particle velocimetry for microscale flows using volumetric scanning," Meas. Sci. Technol. **23**, 085304 (2012).
37. L. Hong, and L. P. Chamorro, "A fast, non-iterative ray-intersection approach for three-dimensional microscale particle tracking," Lab Chip **22**, 964 (2022).
38. F. Pereira, H. Stüer, E. C. Graff *et al.*, "Two-frame 3D particle tracking," Meas. Sci. Technol. **17**, 1680 (2006).
39. M. H. Winer, A. Ahmadi, and K. C. Cheung, "Application of a three-dimensional (3D) particle tracking method to microfluidic particle focusing," Lab Chip **14**, 1443 (2014).
40. R. Barnkob, C. J. Kähler, and M. Rossi, "General defocusing particle tracking," Lab Chip **15**, 3556 (2015).
41. T. Fuchs, R. Hain, and C. Kähler, "In situ calibrated defocusing PTV for wall-bounded measurement volumes," Meas. Sci. Technol. **27**, 084005 (2016).
42. T. Fuchs, R. Hain, and C. J. Kähler, "Non-iterative double-frame 2D/3D particle tracking velocimetry," Exp. Fluids **58**, 119 (2017).
43. M. Novara, D. Schanz, N. Reuther *et al.*, "Lagrangian 3D particle tracking in high-speed flows: Shake-The-Box for multi-pulse systems," Exp. Fluids **57**, 1 (2016).
44. E. Cowen, S. Monismith, E. Cowen *et al.*, "A hybrid digital particle tracking velocimetry technique," Exp. Fluids **22**, 199 (1997).
45. A. Stitou, and M. L. Riethmuller, "Extension of PIV to super resolution using PTV," Meas. Sci. Technol. **12**, 1398 (2001).
46. P. Cornic, B. Leclaire, F. Champagnat *et al.*, "Double-frame tomographic PTV at high seeding densities," Exp. Fluids **61**, 23 (2020).
47. S. Shi, J. Ding, C. Atkinson *et al.*, "A detailed comparison of single-camera light-field PIV and tomographic PIV," Exp. Fluids **59**, 46 (2018).
48. M. Broxton, L. Grosenick, S. Yang *et al.*, "Wave optics theory and 3-D deconvolution for the light field microscope," Opt. Express **21**, 25418 (2013).

49. K. Ohmi, and S. P. Panday, "Particle tracking velocimetry using the genetic algorithm," J. Vis. **12**, 217 (2009).
50. P. Jia, Y. Wang, Y. Zhang *et al.*, "Relaxation algorithm-based PTV with dual calculation method and its application in addressing particle saltation," J. Vis. **18**, 71 (2015).
51. F. Scarano, "Tomographic PIV: principles and practice," Meas. Sci. Technol. **24**, 012001 (2012).
52. R. Prevedel, Y.-G. Yoon, M. Hoffmann *et al.*, "Simultaneous whole-animal 3D imaging of neuronal activity using light-field microscopy," Nat. Methods **11**, 727 (2014).
53. K. Yu, and J. Xu, "Adaptive PIV algorithm based on seeding density and velocity information," Flow. Meas. Instrum. **51**, 21 (2016).
54. A. Rubbert, and W. Schröder, "Iterative particle matching for three-dimensional particle-tracking velocimetry," Exp. Fluids **61**, 58 (2020).
55. M. Raffel, C. E. Willert, F. Scarano *et al.*, *Particle image velocimetry: a practical guide* (Springer, Berlin, 2018).